Tropospheric Waveguide Teleconnections and Their Seasonality

GRANT BRANSTATOR AND HAIYAN TENG

National Center for Atmospheric Research,[a] *Boulder, Colorado*

(Manuscript received 24 October 2016, in final form 10 February 2017)

ABSTRACT

One-point correlation maps of the subseasonal variability of 200-hPa meridional wind in nature and an atmospheric general circulation model are systematically analyzed to quantify the impact of the climatological-mean jets on tropospheric covariability as a result of the jets acting as waveguides for the propagation of Rossby waves. As anticipated by linear theory, signatures of jet influence are detected in terms of (i) the geographical position of the strongest teleconnections, (ii) the zonal orientation and extent of prominent patterns of variability, and (iii) the scale of the features that make up those patterns. Further evidence of jet waveguide influence comes from examining the seasonality of these teleconnection attributes. During winter, covariability can be essentially circumglobal, while during summer it tends to be confined within two separate sectors of the globe where the jets are especially strong. Experiments with a multilevel linear planetary wave model confirm that the analyzed characteristics of teleconnections in the waveguides can be attributed to the action of the mean state; no organization to the anomalous forcing of the atmosphere is required to produce these properties. Some attributes, however, depend on the presence of zonal variations in the climatological-mean state that are of similar scale to the teleconnection patterns themselves.

1. Introduction

In contrast to some well-known teleconnection patterns, such as the Pacific–North America (PNA) pattern and the North Atlantic Oscillation (NAO) (Wallace and Gutzler 1981; Barnston and Livezey 1987), there is a class of intrinsic patterns of subseasonal and longer covariability that are primarily oriented in the zonal direction (Branstator 2002). Planetary wave theory suggests that these teleconnection patterns, which tend to occur in the vicinity of the time-mean tropospheric jets, exist because the strong meridional gradients in absolute vorticity associated with these jets trap perturbation energy, allowing it to propagate only in the zonal direction; the mean jets act as waveguides. Interest in these distinctive patterns is increasing. One reason is that they appear to contribute to various observed phenomena (Branstator 2002; Watanabe 2004; Teng et al. 2013; Harnik et al. 2016) and events (Schubert et al. 2011; Petoukhov et al. 2013). Another is they may be key to understanding how events in one region can impact other, very distant, regions. Indeed, some of these patterns have been called "circumglobal" (Branstator 2002; Ding and Wang 2005).

The first papers that presented observational evidence of the importance of the tropospheric jets as waveguides for teleconnections (e.g., Hsu and Lin 1992; Branstator 2002; Chen 2002) focused on northern winter. Since then, many studies (e.g., Ding and Wang 2005; Kosaka et al. 2009) have found evidence of jet-trapped patterns in northern summer. These studies have provided anecdotal evidence that the character of waveguide-induced teleconnections is not the same in winter and summer, a property that is predicted by theory. In the investigation reported here, we systematically quantify properties of observed and modeled tropospheric teleconnections that should reflect the influence of the waveguides and, in particular, we concentrate on properties that should depend on the season. Our goal is to elucidate the role of the waveguide mechanism in promoting covariability between widely separated regions in the Northern Hemisphere and to learn about mean-state characteristics that contribute to that mechanism.

Our choice of teleconnection properties that will highlight the influence of the waveguides and their seasonality is guided by linear planetary wave theory.

[a] The National Center for Atmospheric Research is sponsored by the National Science Foundation.

Corresponding author e-mail: Grant Branstator, branst@ucar.edu

DOI: 10.1175/JAS-D-16-0305.1

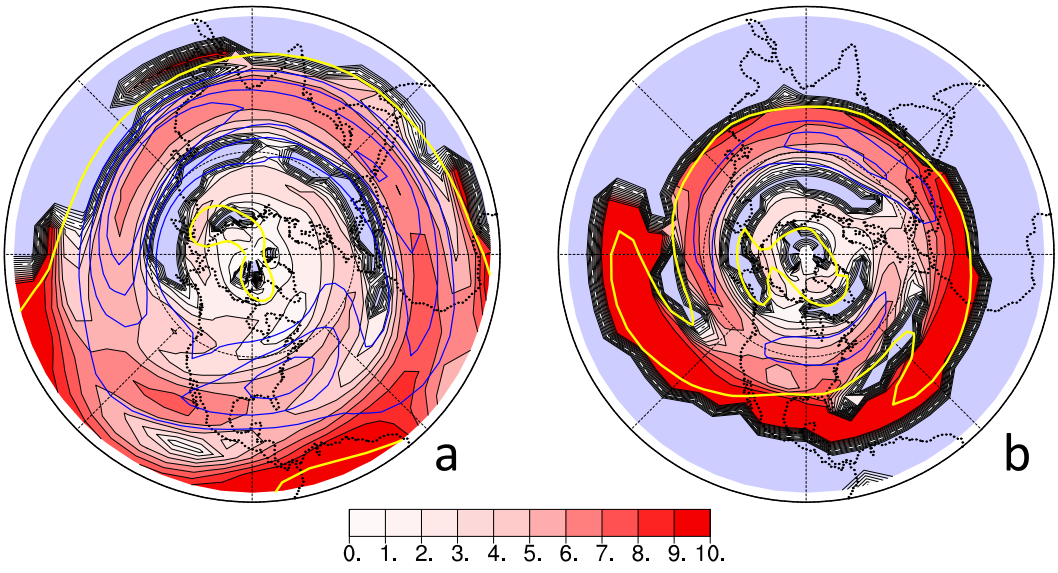

FIG. 1. Climatological-mean u200 from reanalysis data (contours) and stationary wavenumber (color-filled contours) for (a) DJF and (b) JJA as derived from the expression given by Hoskins and Karoly (1981) applied to mean u200. The u200 contours are at −5 (yellow), 20, 30, 40, and 50 m s^{-1}. Light blue designates regions with imaginary stationary wavenumbers.

The original theory for Rossby waves (Rossby 1939) is especially well suited for explaining some characteristics of these waveguide teleconnections, for it concerns disturbances that only vary in the zonal direction. This theory indicates the strength and scale of low-frequency disturbances (and associated teleconnection patterns) should be noticeably different in winter and summer. As Hoskins (1983) has pointed out, if one uses the analysis of the one-dimensional linear barotropic vorticity equation given by Rossby (1945) and Yeh (1949), then it can be shown that, for a steady point source of vorticity at zonal location $x = 0$, the response of the meridional wind at location x will be proportional to $\exp(-dx)\sin(kx)$, where $d = \alpha/(2u_0)$ and $k = [(4u_0\beta^* - \alpha^2)^{1/2}]/(2u_0)$. If one picks values that are representative of the climatological upper-tropospheric jets for background zonal wind u_0 and the meridional gradient of absolute vorticity β^* and a damping rate $\alpha = (5 \text{ days})^{-1}$, then the zonal wavenumber is about 5 for midlatitude winter conditions and 6 for summer. Moreover, the decay rate d for winter is much weaker than for summer, which is a consequence of the group velocity for stationary waves being $2u_0$ in this model.

This one-dimensional theory can be generalized, as was done by Hoskins and Karoly (1981), to produce a linear theory for Rossby waves in two dimensions by placing it on the sphere and incorporating a basic state that is a function of latitude. Branstator (1983) and Hoskins and Ambrizzi (1993) pointed out that this framework can be applied locally to a system with a basic state that also varies zonally provided those variations are gradual. In this context, a key quantity is the so-called stationary wavenumber $K_s = (\beta_M^*/u_M)^{1/2}$, where the meridional gradient of background absolute vorticity β_M^* and the background zonal wind u_M are expressed in Mercator coordinates. The stationary wavenumber K_s gives the total wavenumber of free stationary-plane Rossby waves and also serves as a refractive index for them. When we plot K_s in Fig. 1 for the climatological-mean conditions during December–February and June–August, we see the potential for even greater seasonal contrasts in waveguide teleconnections than expected from the one-dimensional theory. On these plots, the waveguides show up as local maxima in refractive index K_s (Hoskins and Ambrizzi 1993; Ambrizzi et al. 1995), so the plots indicate that both the latitudinal and longitudinal location of waveguide-induced teleconnections are likely to be different for winter and summer. As was true for the one-dimensional theory, Fig. 1 also indicates the dominant scales of these teleconnections should depend on season and location. Furthermore, since the zonal group velocity continues to be proportional to the local background zonal wind in the two-dimensional theory, the very long winter subtropical Asian jet is likely to produce teleconnections between much more widely separated regions than occur in summer, when the two subtropical jets are weaker and shorter.

From the above considerations, one would expect the location, strength, zonal extent, and scale of teleconnections in the vicinity of the mean jets to be affected

by the waveguiding action of these jets and that these properties should be seasonally dependent. In sections 3 and 4 of this paper, we investigate these four properties for subseasonal variability in nature and in an atmospheric general circulation model, and we find qualitative agreement with the influence of the mean jets predicted by linear theory. In section 5, we confirm the connection between mean-state properties and teleconnection characteristics through experiments with a linear planetary wave model and determine which aspects of the mean state are essential for producing the observed teleconnection characteristics. Section 6 summarizes and discusses these results.

2. Data and models

We base our study on one-point correlation plots, reasoning that correlations give a reliable indication of covariability. By contrast, variance-maximizing techniques, like empirical orthogonal functions (EOFs), can suggest connections between locations that do not actually covary (Deser 2000; Ambaum et al. 2001). The field whose covariability we examine is v200, the nondivergent meridional wind at 200 hPa. As explained in appendix A, we use v instead of geopotential or streamfunction, because v should emphasize the jet-trapped, zonally oriented, geographically extended patterns we are interested in. As is true for all fields in our study, we use v200 that is truncated to R15.

When analyzing the properties of teleconnections in nature, we use daily NCEP/NCAR reanalysis fields for the years 1958–2014. To isolate subseasonal time scales for this dataset, we usually employ 20-day averages with centered 90-day averages removed. Using 20-day rather than monthly means is part of our strategy for producing robust results despite the shortness of this record. (In results not shown here, we have found that the shorter averaging time decreases the strength of teleconnections but only slightly.) Usually we consider 100-day seasons consisting of five 20-day averages. For example, the DJF season consists of the five 20-day averages that begin on 1 December.

We also analyze a 1000-yr integration of a T42, 26-level version of the CAM5 AGCM (Hurrell et al. 2013; Kay et al. 2015), which was run with climatological-mean sea surface temperatures (SSTs) that are only a function of the day of the year. For those data, we concentrate on the characteristics of individual months by considering 30-day averages of v200 with centered 90-day means subtracted.

The design of our analysis of these datasets is motivated by the theories mentioned in the introduction, but we are only able to make a qualitative comparison to theory. Furthermore, with its assumption of slow mean-state spatial variations and difficulties inherent in drawing conclusions about the global properties of perturbation fields from the local properties given by the theory—for example, accounting for those resonances that can occur because of the cyclic nature of the sphere (Manola et al. 2013)—the theory does not incorporate the entire range of effects that the mean state and its jets can linearly have on perturbations. For these reasons, we carry out experiments with a linear model that allow for a quantitative comparison of teleconnection properties to the behavior produced by complete linearized dynamics. Others have used linearized barotropic vorticity equation models to make qualitative comparisons (Ambrizzi et al. 1995; Newman and Sardeshmukh 1998; Branstator 2002; Branstator and Frederiksen 2003; Ding et al. 2011) and to study seasonality (Branstator and Frederiksen 2003; Newman and Sarkeshmukh 1998). Here, to make the dynamics more comprehensive, we use a linearized multilevel primitive equation model that is similar to that described by Branstator (1990), except for the number (namely, 12) and placement of levels, the horizontal truncation (R15), and the values of damping coefficients [$(6\text{ days})^{-1}$ for all fields with vertical coordinate σ less than 0.850 and $(1\text{ day})^{-1}$ elsewhere].

We assume that analyzing steady solutions to this model gives the information we require concerning its characteristics on the time scales represented in our analysis of nature and CAM5. For a given basic state, we generate 5000 such solutions, each of which is forced by a different distribution of combined steady temperature and vorticity sources. These solutions are found through direct solution of the steady equations rather than through time integrations, which would be dominated by baroclinically unstable modes. Each forcing distribution is produced by assigning values generated by random draws from a Gaussian distribution to each point on the model three-dimensional grid. The temperature and vorticity components of the forcing fields are normalized separately in such a way that, for the 5000 solutions, the contribution of these two components to the aggregate global variance of v at $\sigma = 0.200$ (which is the variable we analyze for this model) is equal. By using randomly generated forcing, we ensure that any organization we find in the 5000 solutions is necessarily the result of the combined effect of the model dynamics and the basic state and not because of systematic forcing inhomogeneities.

3. Teleconnection properties in nature

a. Leading patterns

To examine teleconnections in nature for winter, we construct 960 one-point correlation maps using 20-day averages during DJF. Each one has a base point at a different Northern Hemisphere (NH) location on an R15 transform grid. As a measure of the strength of each of these maps, we calculate its area-weighted RMS in

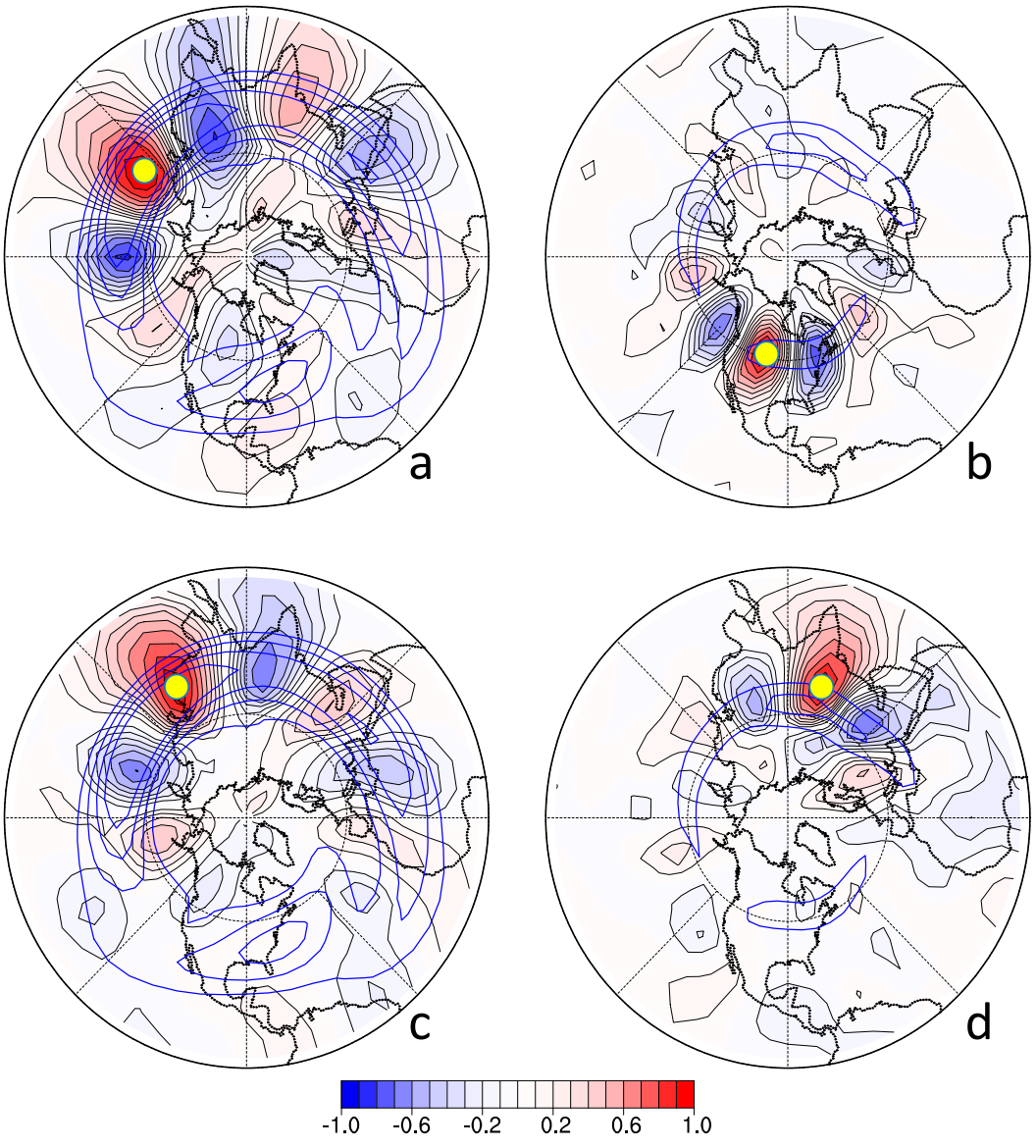

FIG. 2. Leading one-point correlation maps of subseasonal fluctuations of 20-day-mean reanalysis v200 during (a) DJF and (b) JJA and second-leading maps for (c) DJF and (d) JJA. Yellow dots mark the base points. Overlaid blue contours are climatological-mean u200 at 20, 30, 40, and 50 m s^{-1}.

the region north of 20°N. We refer to this as the *extended teleconnectivity* (xTC) of the map's base point. In contrast to *teleconnectivity* (Wallace and Gutzler (1981), xTC takes into account the strength of covariability with the entire northern extratropics.

Of the midlatitude base points between 25° and 60°N, the one with largest xTC is located at 33.3°N, 142.5°E. The strongest features on the associated map (Fig. 2a) are near the core of the Asian subtropical jet and vary primarily in the zonal direction. It extends more than three-quarters of the way around the globe and corresponds to a pattern that Branstator (2002) referred to as being circumglobal. Many other one-point correlation maps have similar structures, but if we use a least squares fit to the Fig. 2a pattern to remove it from each of the DJF one-point correlation charts and recalculate the xTC of each of the resulting maps, we find the base point with greatest xTC is located at 29.0°N, 120.0°E. When we plot it (without removing the Fig. 2a pattern) in Fig. 2c, we see that it too is in the Asian waveguide and nearly circumglobal, though the front of the wave train does not extend as far into the tropics. By construction it is approximately in spatial quadrature with the first pattern. Together these two leading patterns

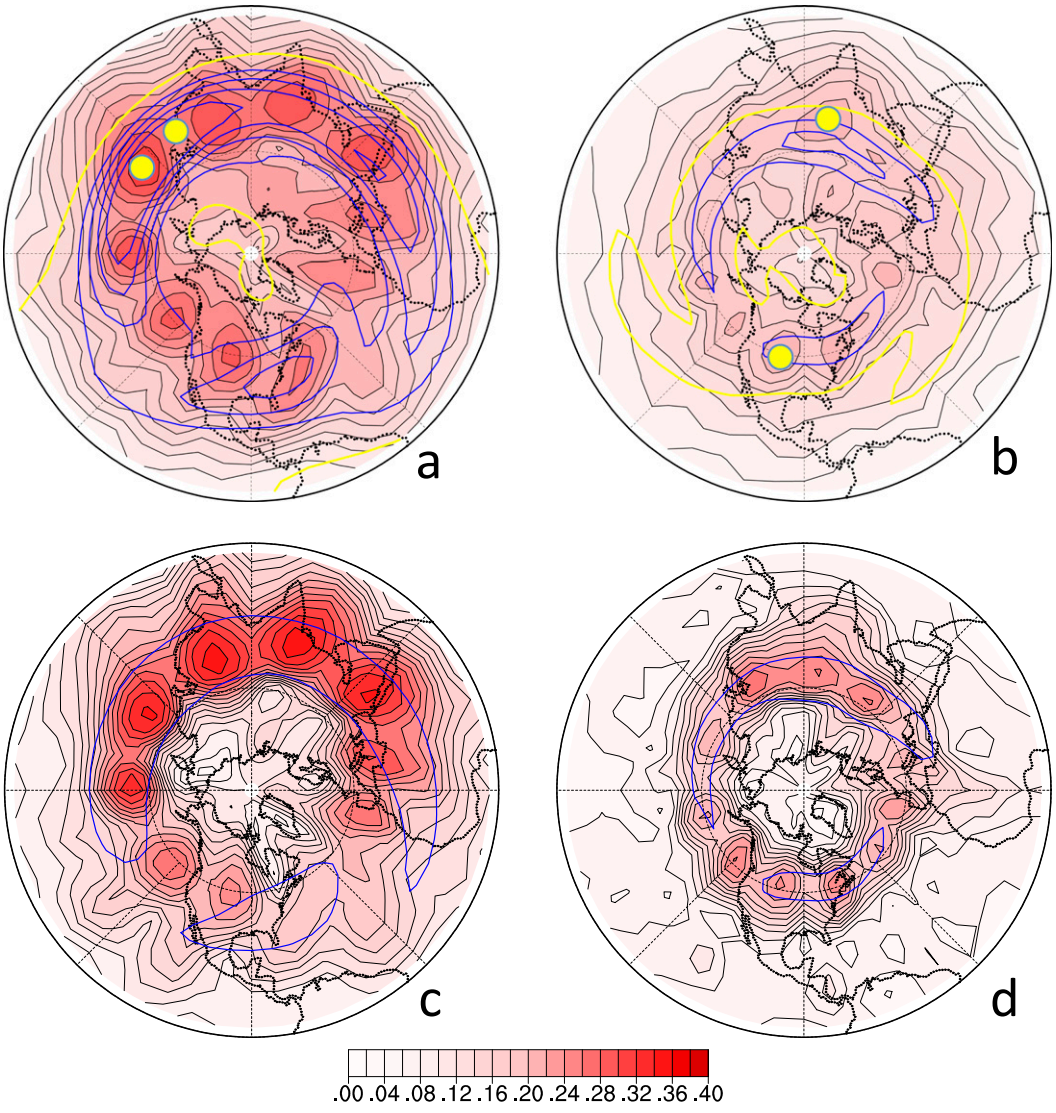

FIG. 3. (top) Extended teleconnectivity of subseasonal fluctuations of 20-day-mean reanalysis v200 for (a) DJF and (b) JJA. Overlaid are contours of climatological-mean u200 as in Fig. 1. Yellow dots are the base points of the leading one-point correlation maps plotted in Fig. 2. (bottom) RMS of all one-point correlation maps with base points within the core of the mean jets (blue contours) for (c) DJF and (d) JJA (see the text for details).

explain 49% of the extratropical variance of the correlation maps with midlatitude base points, an indication of the importance of waveguide-influenced patterns.

Figures 2b and 2d display the leading two one-point correlation maps for JJA. They too are patterns whose main variations are primarily in the zonal direction and near the mean jets. Unlike for DJF, the two are on opposite sides of the globe, with the first pattern having a base point at 46.7°N, 105.0°W, and the second pattern having a base point at 33.3°N, 75.0°E. Also, their lobes have smaller zonal scales than the DJF patterns, corresponding to approximately zonal wave 6 rather than 5. And they are not nearly as circumglobal, though if one includes the low-correlation features in the Eastern Hemisphere, this designation could be appropriate for the leading JJA pattern. Together, these patterns represent 41% of the extratropical variance of JJA correlation maps with midlatitude base points.

b. *Strength*

Recognizing the high degree to which the leading patterns in Fig. 2 conform to the expected properties of waveguide-influenced behavior, we next look more systematically for these same properties by employing specially designed metrics. First, we consider the strength of teleconnections as given by xTC. When we plot xTC of each

DJF NH one-point correlation map at its base point, the chart in Fig. 3a results. Note this is equivalent to plotting at each NH grid point the RMS of correlations at that location from all one-point correlation maps with base points north of 20°N, weighted by the cosine of their base points.

From Fig. 3a, it is apparent that the points with strongest connections to the rest of NH midlatitudes are concentrated in a rather narrow midlatitude band. This band stretches completely around the globe, but the very strongest teleconnections are for maps with base points in the sector that extends from about 45°E to 180°. Referring to the contours of mean u at 200 hPa (u200) that are superimposed (and K_s values in Fig. 1a), this sector is where the waveguide trapping is strongest and where teleconnection patterns should be especially broad in the zonal direction. There is also some suggestion that the northward spiraling of the points with strongest teleconnections over the North Atlantic corresponds to the northward bending of the jet there. Another noteworthy feature within the midlatitude band is the local regions of relatively high xTC that are separated by 30° or 40° of longitude, resulting in 10 regions of especially high xTC. The examples in Figs. 2a and 2c (whose base points are marked with yellow dots in Fig. 3a) give some idea of how different the strengths of waveguide teleconnection patterns are, depending on whether they are associated with one of these special regions.

Comparing a plot of xTC for JJA in Fig. 3b to the DJF plot of xTC, we see indications of strong seasonality in waveguide teleconnections. As with DJF, there is a latitudinal band with above-average xTC, but it is closer to the pole, consistent with the mean jet being more poleward, and overall xTC is weaker. Also, rather than there being especially strong xTC in one broad sector, there is a suggestion of two sectors with above-average xTC: one over Asia and another over North America and the North Atlantic. Within these sectors there are also some longitudinal variations, but they are not as apparent as for DJF, and the statistical significance of the variations is difficult to establish with these data.

For the examples in Fig. 2, base points in the waveguide covary almost exclusively with other points in the waveguide. To determine whether this is true more generally, we calculate a modified version of Figs. 3a and 3b. We only consider one-point correlation maps for base points within the mean jets, which we take to be points with mean zonal winds greater than 30 m s^{-1} in winter and 20 m s^{-1} in summer. And we set to zero their values at all points within 15° longitude of the base point so that these correlations, which are not an indication of remote covariability, do not affect our results. When for DJF we calculate at each grid point the RMS of this collection of maps, we find (Fig. 3c) that the points that tend to covary with base points in the jet are also within the latitude band of the waveguide. Similar statements hold for JJA (Fig. 3d). Note also that the RMS values within the waveguides are even stronger than in the previous plots, even though the high correlation values near the base points are not contributing, further confirming the especially strong teleconnections between points in the waveguides. These panels also make the zonal variations of teleconnection strength within the waveguides even more apparent than the plots of xTC, and comparison with Fig. 2 makes it clear that the local maxima are a reflection of the leading one-point correlation patterns.

c. *Span*

The extended teleconnectivity does not give a measure of how broad a region the highly correlated points in a given one-point correlation map are spread over. One reason to be interested in the geographical extent of teleconnection patterns is to determine to what extent the term ''circumglobal'' is justified. To address this issue, we have devised a measure, which we call *span*. For a given one-point correlation map, it is the sum of 1) the distance in the zonal direction between the base point and the farthest location to its west that surpasses some threshold value of absolute correlation and 2) the distance between the base point and the farthest location to its east that exceeds the same threshold. When determining these two locations, only grid points between 20° and 60°N are considered, and they must be part of a chain of regions with high absolute correlations that has no gaps greater than 45° longitude wide where values are below the threshold. In the plots of span in this paper, a threshold of 0.35 is employed.

When we plot the span for DJF (Fig. 4a), we see the same general properties revealed by xTC. In winter, the one-point correlation maps with broadest zonal extent occur for base points that are near the waveguide and tend to be in regions where the jet is strongest. For some of these locations (e.g., the Fig. 2a map), it has values in excess of 24 000 km. Considering that the globe's circumference is about 32 000 km at the latitude of these locations, ''circumglobal'' is an apt term.

For JJA (Fig. 4b), the geographical distribution of span is not as well organized as for DJF, but there is an indication of larger-than-average values where the mean jets are strongest, especially over North America. Our definition of span is sensitive to small details in a given one-point correlation plot, which leads to the rather noisy plot for JJA, with its weak correlations. What is clear is that for points in the waveguide the spans during

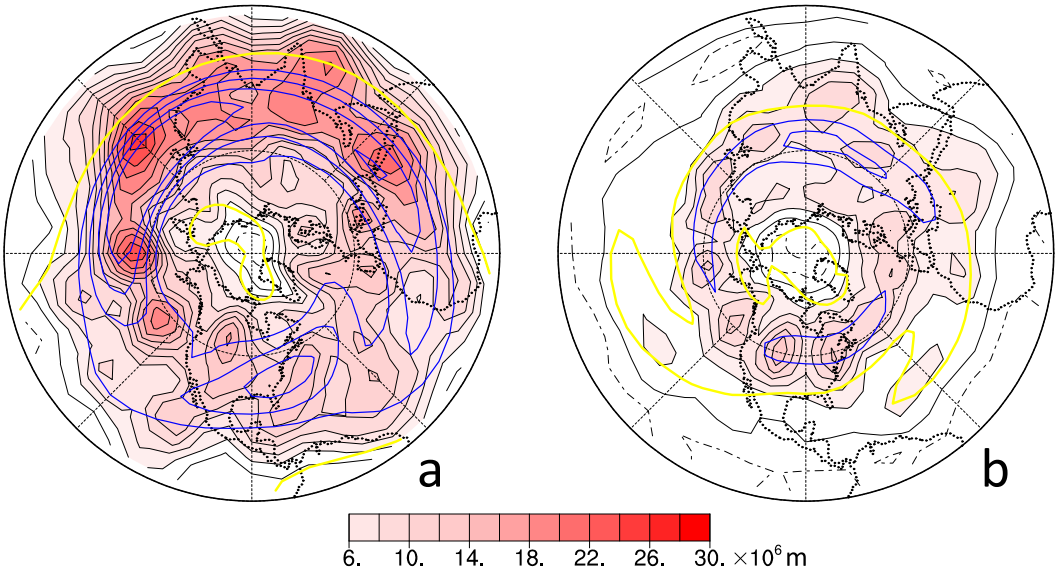

FIG. 4. Span of one-point correlation maps (color-filled contours) of subseasonal fluctuations of 20-day-mean reanalysis v200 plotted at the location of the base point of each map for (a) DJF and (b) JJA. Overlaid are contours of climatological-mean u200 as in Fig. 1.

summer are much shorter than for winter, and "circumglobal" is not nearly as appropriate a designation.

d. Zonal scale

The additional attribute of waveguide teleconnections that the linear theory outlined in the introduction indicates should depend on season is the scale of variations on one-point correlation plots. The one-dimensional theory concerns zonal scales, while the stationary wavenumber from two-dimensional theory concerns total wavenumber. Here, for ease of analysis and because, when we examine examples of one-point correlation charts (e.g., Fig. 2) we notice evidence that the waveguides are affecting scale in the zonal direction, we focus our analysis on zonal scales.

A straightforward method to consider zonal scale is to apply Fourier analysis to each latitude of one-point correlation maps. Again employing seasons consisting of five 20-day means, we do this for each reanalysis correlation map that has a base point north of 20°N. Figure 5 shows the mean squares of these amplitudes as a function of latitude and zonal wavenumber for NH winter and summer. As anticipated by the one-dimensional theory, the most prominent wavenumber is 5 near the core of the winter jet at about 30°N. On the other hand, during summer the leading wavenumber is 6 in the vicinity of the jet core at about 45°N.

For later application, we point out that the seasonal contrasts in scale near the jets in Fig. 5 are embedded in a more general shift in scale that is reflected in the slope of the distribution of variance in these plots, with a much stronger negative slope occurring during DJF than during JJA. This can be traced to very basic dynamics that do not involve meridional trapping. The stationary wavenumber (Hoskins and Karoly 1981) for the solid-body rotation component of climatological u200 is $K_s^{\mathrm{SBR}} = [(2/u_{\mathrm{eq}}^{\mathrm{SBR}})(\Omega/a_e + u_{\mathrm{eq}}^{\mathrm{SBR}}/a_e^2)]^{1/2}\cos(\varphi)$, where a_e is Earth's radius, Ω is the rotation rate, φ is latitude, and $u_{\mathrm{eq}}^{\mathrm{SBR}}$ is the equatorial speed of the solid-body-rotation component. Plotting K_s^{SBR} with solid lines in Fig. 5, one sees—keeping in mind that stationary wavenumber concerns total wavenumber—that the seasonality of this component is a major factor in the seasonal shift in teleconnection spectral characteristics.

Expecting the impact of the mean state, particularly the mean jets, to produce not only a latitudinal dependence on the scales of one-point correlation map features but also a longitudinal dependence, we devise a second indicator of zonal scale that is a function of latitude–longitude index (j, i). For each point (j, i), we find all maps for which the absolute value of the correlation at (j, i) is greater than 0.3. On each map, such a point is surrounded by a region of similarly signed correlations. We find the zonal width of that region by locating the nearest longitudes due west and east of the point where the correlation is zero and transform the distance between these two locations into a zonal wavenumber and associate it with (j, i). Averaging all such wavenumbers for (j, i) while taking into account a weight that reflects the base point latitude of contributing maps, we arrive at the local zonal wavenumber for location (j, i).

When we calculate zonal scales for DJF and JJA in this way, Figs. 6a and 6b result. For DJF the influence of the waveguide is clear, with scales across northern

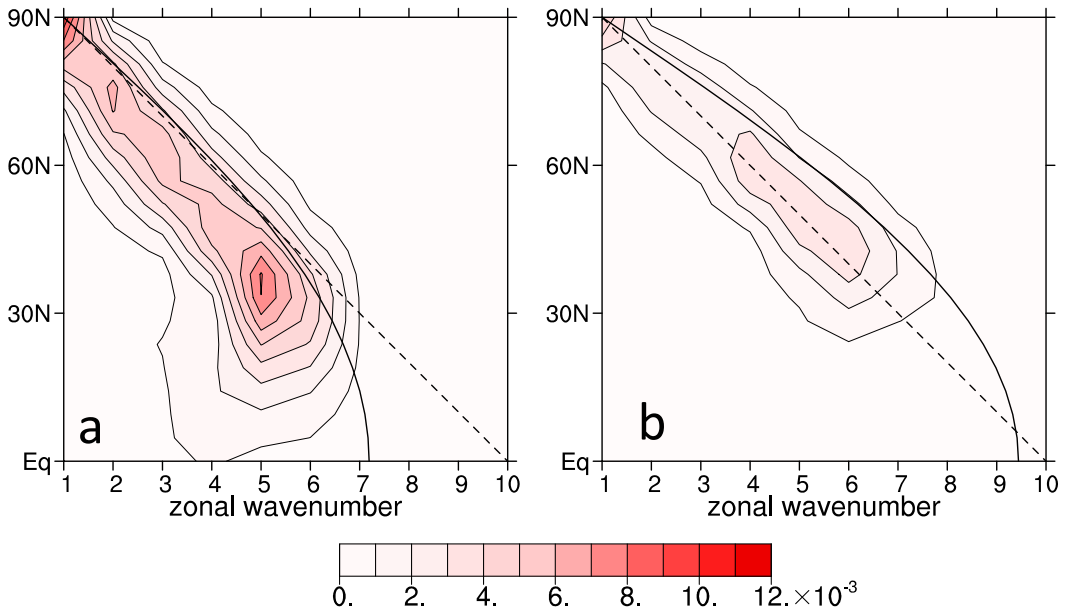

FIG. 5. Mean square Fourier amplitude of all one-point correlation maps with base points north of 20°N for subseasonal fluctuations of reanalysis 20-day-mean v200 during (a) DJF and (b) JJA. The thick solid line is the stationary wavenumber for the solid-body component of zonal-mean, climatological-mean u200. The dashed line on the diagonal is to facilitate comparison of panels.

Africa, Asia, and the western North Atlantic at approximately the latitude of the mean jet having larger wavenumbers than at latitudes to the north and south. Similarly, across Africa and Asia but farther to the north, there is a band of high wavenumbers for JJA. For our study what is particularly noteworthy is that in virtually every region that is influenced by the mean jets, wavenumbers in JJA are larger by about 1 than they are in winter. We see that there are also prominent features on these plots, particularly in the subtropics, that are consistent with linear theory (Fig. 1) but that do not correspond to the midlatitude jets.

As described above, the shape of the globe and the solid-body-rotation component of the mean state are responsible for the general decrease in wavenumber that is observed the closer a point is to the pole. Through trial and error we have found that an approximate way to remove this simple component from the distributions in Figs. 6a and 6b is to assume that the zonal wavenumbers produced by this effect are half of the value of the solid-body-rotation stationary (total) wavenumber and subtract them from the distributions. This procedure reveals additional subtle indications of the impact of the waveguides that are masked by the solid-body-rotation component (Figs. 6c,d). Specifically the existence of small-scale teleconnection features in a band at high latitudes of the North Pacific and in tongues stretching northeastward from central North America to high latitudes of the North Atlantic is apparent in both seasons. These features are collocated with regions where the mean jet is prominent.

4. AGCM teleconnections and the seasonal cycle

We would like to consider the complete seasonal cycle by calculating xTC for each month of the year. However, as demonstrated in appendix B, for individual months the reanalysis dataset is too short to estimate xTC with sufficient certainty. Therefore, we analyze the much longer AGCM dataset.

First, we calculate xTC for January and July monthly means. (Results for December–February and June–August are similar in structure, though slightly weaker, which supports our use of 3-month datasets when analyzing these particular seasons for nature in the previous section.) As shown in Figs. 7a and 7c, most of the attributes we noticed for xTC in nature are seen in this simulation. The strongest teleconnections are for base points near the core of the mean jets in both seasons. In fact, this property is even more apparent with the larger dataset, especially for JJA. Also, covariability is much stronger for winter than summer, and the strongest winter teleconnections occur in one broad swath, while for summer the separation of the strongest teleconnections into two longitudinal sectors is more apparent than it was for nature because of a more distinct minimum centered near the date line. Moreover, in both seasons within the waveguides there are alternating regions of relatively

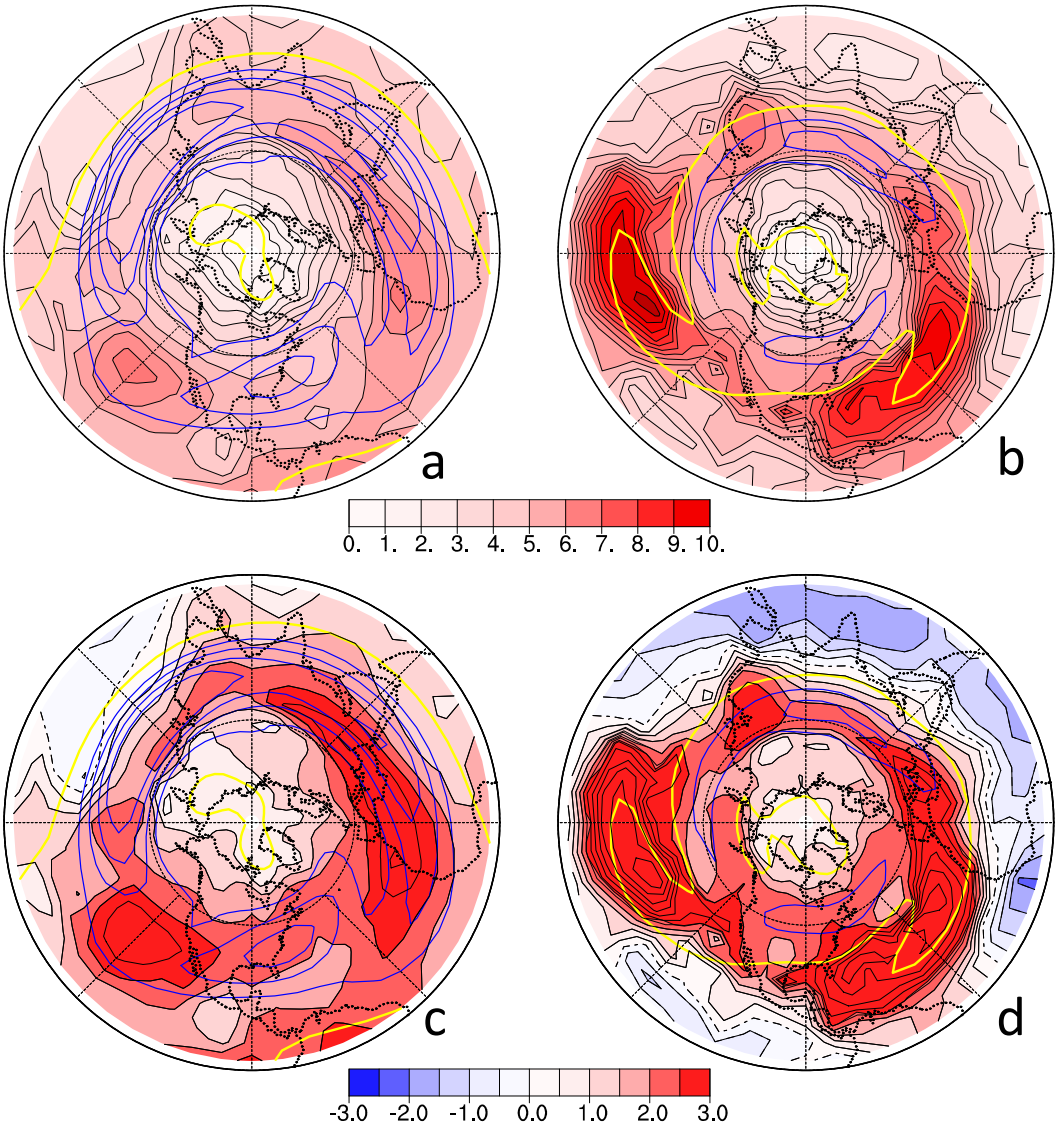

FIG. 6. Average local zonal wavenumber (color-filled contours) of one-point correlation maps for subseasonal fluctuations of 20-day-mean reanalysis v200 during (a) DJF and (b) JJA as calculated using the method described in the text. Overlaid are contours of climatological-mean u200 as in Fig. 1. (c),(d) As in (a) and (b), respectively, but with values derived from the stationary wavenumber of solid-body rotation subtracted. Note in (c) and (d) that contours extend beyond values plotted on the color bar.

high and low xTC, and even the geographical position of these features is very similar in the model and nature.

Based on these results, we conclude it is valid to use the AGCM to examine the seasonal cycle. Examining xTC for April (Fig. 7b) and October (Fig. 7d), we see that during these transition months the strongest teleconnections remain confined to the latitudes where the mean jets are strongest. Interestingly, there are strong contrasts between the two transition months with regions of unusually strong xTC in virtually every longitudinal sector of April while during October the strongest xTC is for base points in a sector that is centered on the date line. Furthermore, the October swath of high xTC is at higher latitudes than it is for April. [Plots of xTC for March–May and September–November from reanalysis data (not shown) indicate similar attributes, though, as we shall see, combining data from three months during these seasons may be misleading.]

To study seasonality in more temporal detail, in Fig. 8 we summarize xTC for each month of the year in two ways. In one approach, we reduce two-dimensional monthly maps of xTC to one dimension by calculating the RMS of these values along each latitude circle

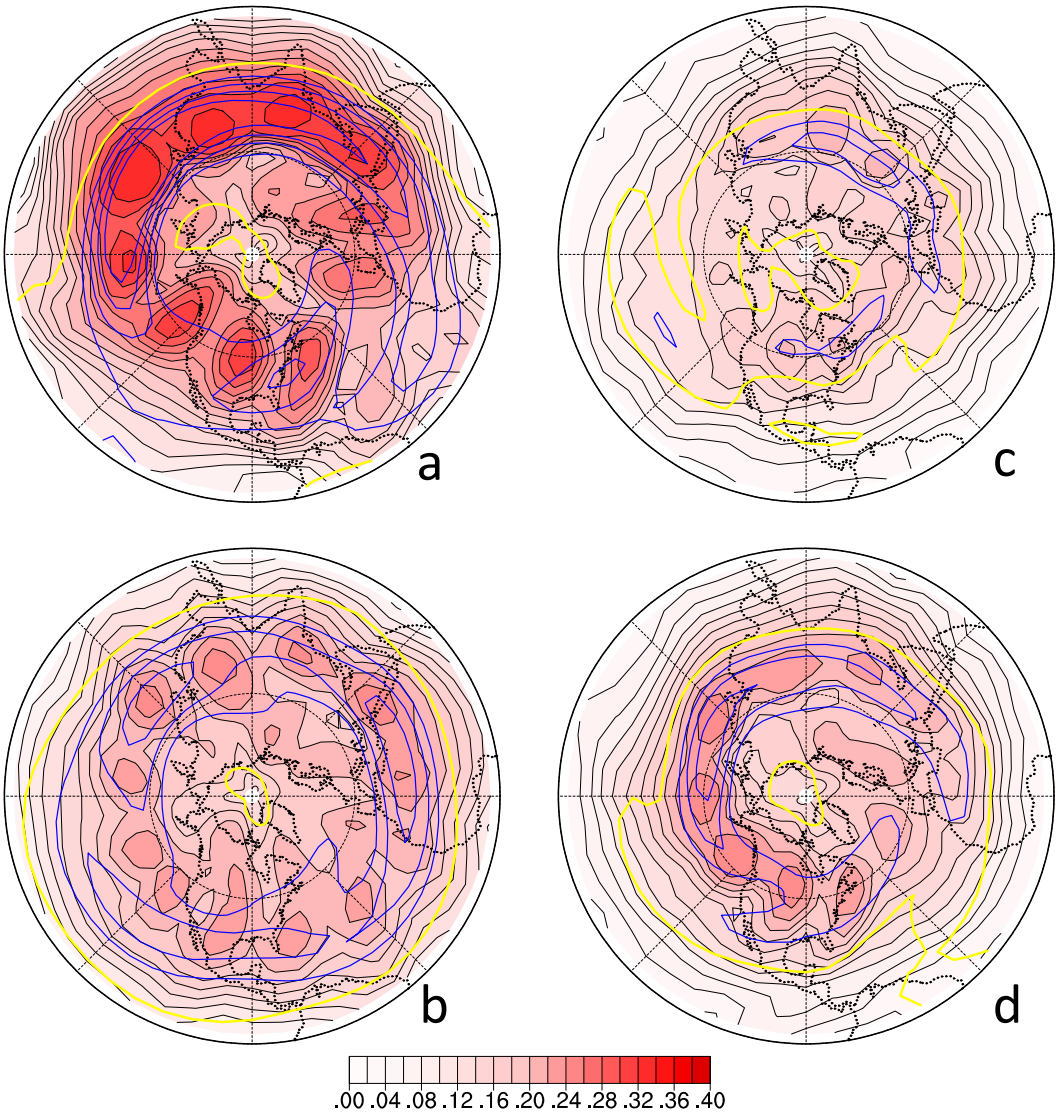

FIG. 7. Extended teleconnectivity for subseasonal fluctuations of 30-day-mean CAM5 v200 for (a) January, (b) April, (c) July, and (d) October. Overlaid are contours of climatological-mean u200 based on the CAM5 dataset.

(Fig. 8a). The concentration of highest xTC near the latitude of the concurrent mean-jet core is apparent, as is the very strong contrast between winter and summer values. Another feature of note is the much more rapid temporal change in values that occurs in midlatitudes during spring and fall than occurs during winter and summer. This is another indication that our decision to analyze 3-month seasons during nature's winter and summer was well founded and also cautions against applying such a strategy to spring and fall. Finally, we note that the contrast in the latitude of prominent xTC noted for April and October is generally valid for all of spring and fall; the latitude of highest xTC is relatively low in spring, while for fall it remains at the high latitude established in summer until about November.

The second way we portray the seasonal cycle is to look at how the longitudinal variations in xTC vary from one month to the next by plotting the latitudinal average of xTC values between 20° and 60°N (Fig. 8b). This plot indicates that summer's property of having its strongest xTC separated into two regions distinguishes it not only from winter but also from spring and fall. Another striking feature is how anchored the regions of locally enhanced xTC are to specific longitudes that change only gradually between October and May and between June and August. Ignoring for the moment the distinctions between spring and fall evident in Figs. 7 and 8a, one might conclude that the structure of xTC within the waveguide has just two seasons—one in summer and one during the cooler months—during each of which only the strength of covariability is modulated.

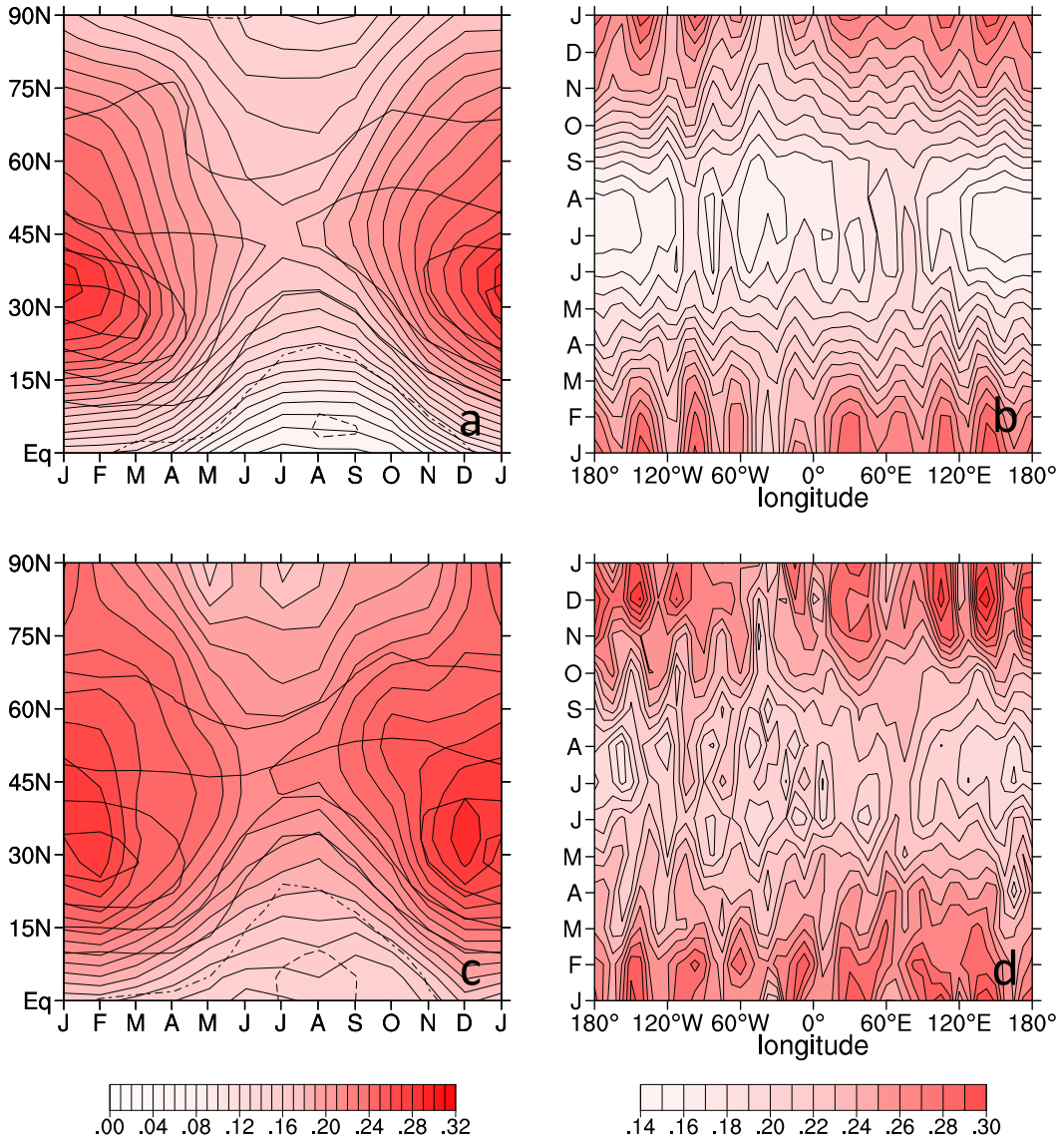

FIG. 8. RMS of extended teleconnectivity at each NH latitude for subseasonal fluctuations of 30-day-mean v200 for (a) CAM5 and (c) reanalysis data. Contours of zonal-mean, climatological-mean u200 are overlaid with a contour interval of 10 m s^{-1}; the dotted–dashed line is the zero contour. Also, extended teleconnectivity averaged for 20°–60°N for the same fluctuations for (b) CAM5 and (d) reanalysis data.

Repeating these seasonal cycle plots using the limited sample of monthly mean v200 from nature, we find that they are qualitatively similar to the corresponding plots for the AGCM dataset. The seasonal march in xTC amplitude is clear in (Fig. 8c), as is the shifting latitude of highest xTC. The anchoring of regions of maximum xTC to the same longitudes throughout fall, winter, and spring is not as definite in nature (Fig. 8d), but these results are too noisy to assess this property (appendix B).

When we examine the spatial scale of one-point correlation plots using CAM5 data in diagrams not shown here, we find very much the same winter versus summer contrasts noted for nature. The one new property we will mention is that, during the transition seasons, the dominant zonal wavenumbers change markedly from one month to the next, which is another indication that analyzing teleconnection characteristics during these seasons by combining months can lead to wrong impressions.

5. Mean-state impacts on teleconnections

For the reasons explained in section 2, we find it worthwhile to carry out a parallel analysis of solutions to a linear planetary wave model. First, we linearize the

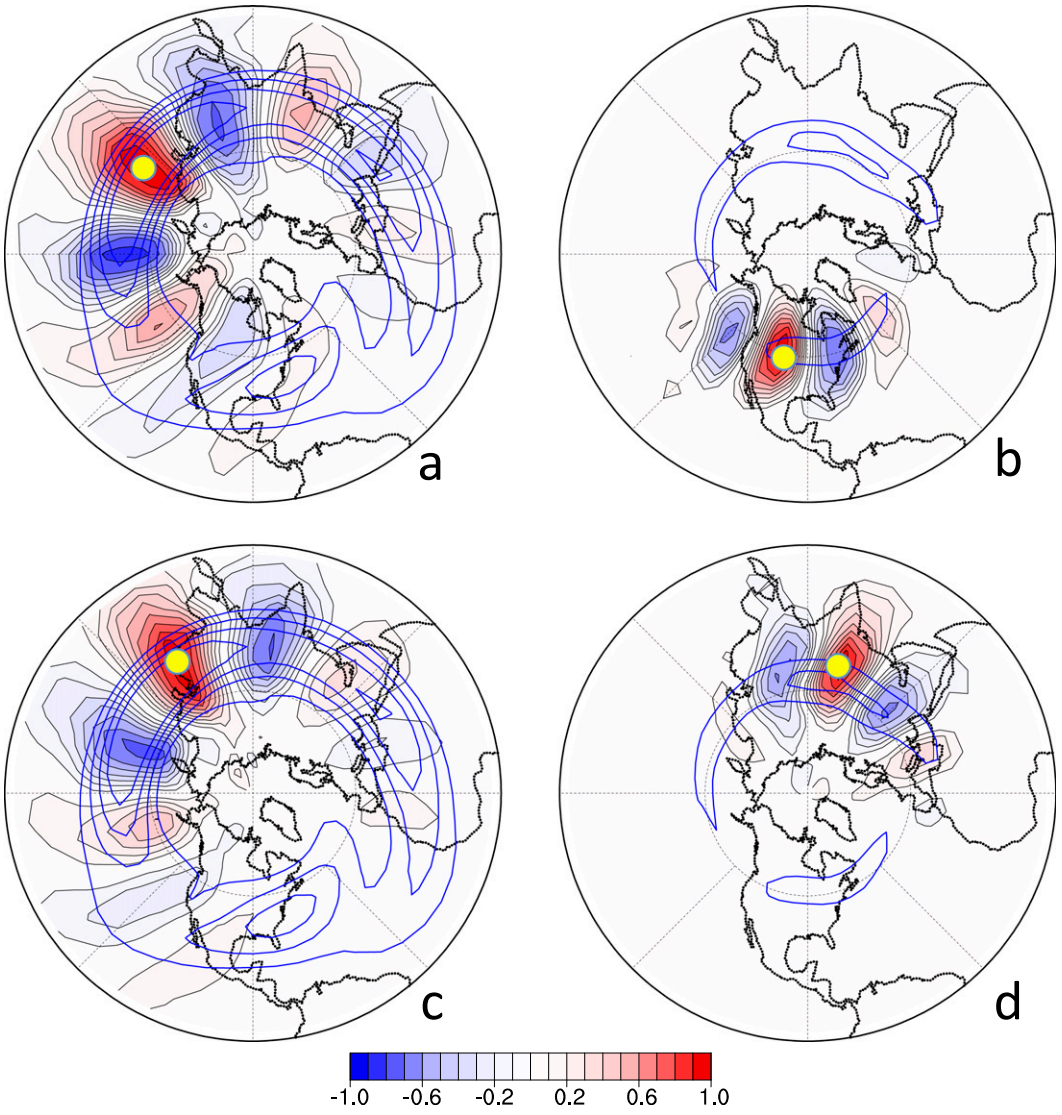

FIG. 9. One-point correlation maps for the same base points and seasons plotted in Fig. 2, but for steady v200 solutions of a stochastically driven linear planetary wave model. Overlaid blue contours are climatological-mean u200 at 20, 30, 40, and 50 m s^{-1}.

model about the DJF and JJA 57-yr mean states from nature and then compare by eye individual one-point correlation plots from these solutions to corresponding maps from nature. We find the similarity is striking, as is demonstrated by the four one-point correlation maps in Fig. 9, which use the same base points as the examples in Fig. 2. Except for the upstream component of the leading JJA pattern (Fig. 9b) and the region of weak correlations over eastern North America and the North Atlantic in the second DJF pattern (Fig. 9c), there is almost a one-to-one match between position, structure, and strength of each high and low in these maps.

Given these similarities, it is not surprising we also find strong similarities in the geographical distribution of xTC during DJF and JJA for the linear solutions (Figs. 10a,c) and nature (Figs. 3a,b), including the preference for strong teleconnections within the waveguides. Even the existence and position of local maxima within the waveguides are reproduced by the linearized dynamics. Perhaps the most apparent discrepancy occurs south of Alaska for JJA, where the linear model does not reproduce two local maxima that are in the plots for nature. However, these features are very weak in the AGCM dataset (Fig. 7c), so they may be a consequence of the short reanalysis time series.

In addition to matching the strong seasonal contrast in xTC between DJF and JJA for nature, we see that the linear model results (Fig. 10) also match the characteristics

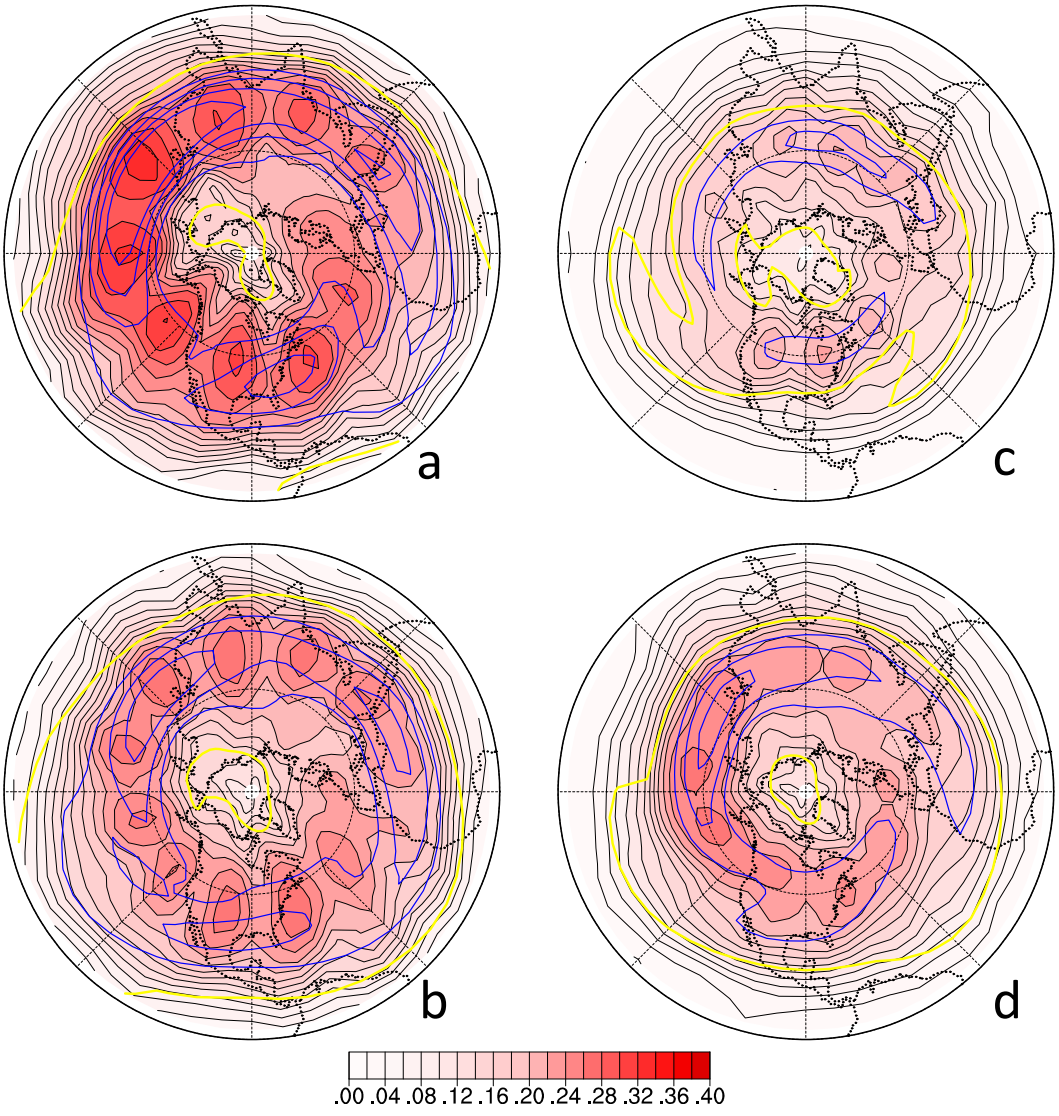

FIG. 10. Extended teleconnectivity for v200 from stochastically driven steady solutions to a planetary wave model when it is linearized about reanalysis climatological-mean conditions for (a) DJF, (b) MAM, (c) JJA, and (d) SON. Overlaid are contours of climatological-mean u200 as in Fig. 1.

for all four seasons of the AGCM simulation (Fig. 7). Even the distinctions between spring and fall are reproduced, including the more poleward placement of the ring of maximum xTC in autumn compared to spring and the more radially symmetric distribution of local maxima in spring compared to autumn. Given the more equatorward and more zonally symmetric configuration of the mean jet seen in Fig. 10 for spring compared to fall, it is perhaps not surprising that the linear model captures these contrasts.

The ability of the linear solutions to reproduce the entire seasonal cycle of AGCM behavior is further confirmed when we look at summarizing plots of month-by-month xTC characteristics. For the zonal RMS of xTC (Fig. 11a), the same seasonality of amplitude and latitudinal distribution are found that exist in the AGCM (Fig. 8a), including the reduction in amplitude by about 35% in summer compared to winter. Equally striking is the ability of the linear dynamics to reproduce the seasonal dependence of the longitudinal distribution of xTC within the band of latitudes where the waveguide exists (Fig. 11b). Summer has two separate regions of relatively high xTC, while the cool seasons have one, and the longitudinal positions of local maxima change only slightly from month to month within each of these two regimes.

The scale of features on one-point correlation plots for the linear solutions also exhibits most of the main properties that are present in nature (and CAM5). For

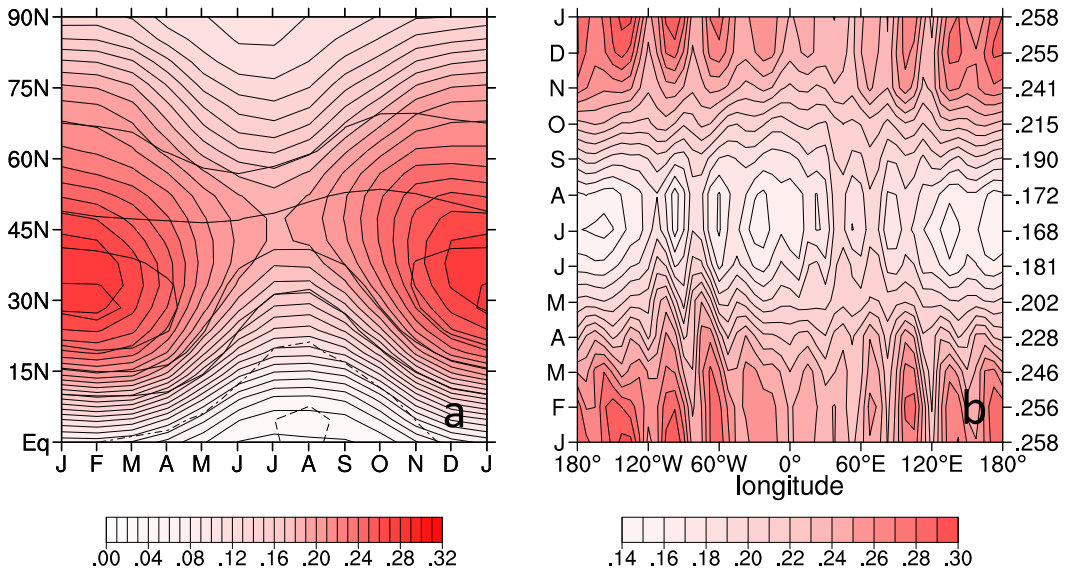

FIG. 11. (a) Zonal-RMS and (b) midlatitude-average extended teleconnectivity, as in Fig. 7, but for v200 solutions to a planetary wave model linearized about each of 12 climatological-mean states, each consisting of a 3-month mean centered on the indicated month.

example, the same winter-versus-summer contrasts in the prevalence of certain zonal wavenumbers at various latitudes occur (Figs. 12a,b vs Fig. 5). These include the dominance of wave 5 at the latitude of the jet core during DJF, the dominance of wave 6 during JJA, and the summer shallowing of the slope of the distribution of amplitude in the latitude–zonal wavenumber plane. Likewise the dynamics of the linearized model generate most of the zonal dependence of local zonal wavenumber (Figs. 13a, b) displayed in the Figs. 6a and 6b diagrams for nature. Even the faint high-latitude local maxima in the North Pacific and between North America and Scandinavia that could only be detected when the component of scale associated with solid-body rotation was removed are reproduced (Figs. 13c,d vs Figs. 6c,d).

The planetary wave model solutions indicate that, while processes other than linearized dynamics may play a role in producing the teleconnection properties we have documented, they are not essential. Their match with nature and CAM5 also introduces the possibility of using the linear model to determine which linearized mechanisms are essential. Here we only investigate the role of small-scale zonal variations in the mean state. We concentrate on this issue because our study is partly motivated by theory that relies on zonal gradients in the mean state being weak.

By repeating the linear experiments with modified basic states, we come to the conclusion that many of the important teleconnection characteristics described above can be produced with basic states that are truncated to include only zonal waves 0, 1, and 2. These characteristics include the concentration of the strongest and broadest teleconnections near the core of the seasonally varying mean jets, as well as the main features of the geographical and seasonal dependence of spatial scales. A chart that serves to quantify this statement with respect to xTC in the waveguides is Fig. 14b, which shows xTC averaged between 20° and 60°N as a function of month of the year for the model with basic states truncated beyond zonal wave 2. When compared to Fig. 8b, it is apparent that most of the gross features are reproduced, including the rapid transition in strength between cold and warm seasons and the accompanying shift from one broad region of high xTC in winter to two narrower regions in summer. The one aspect of the longitudinal dependence of xTC that these truncated basic states do not generate is the small-scale longitudinal variations in xTC amplitude. We find, however, that if we retain at least five zonal waves in the basic states, then those features are produced during the cold season, but even more basic-state waves are needed for their appearance during summer (Fig. 14a). For the zonal scale of variability on teleconnection maps, the situation is similar. Gross geographical variations in these scales, including the preference for small-scale features near the jets, are reproduced with basic states truncated at wave 2, but weak, finer-scale regional features, like those that are only apparent when the background solid-body-rotation-induced features are removed, are missing (not shown).

To further determine the importance of mean-state zonal variations, we examine solutions for basic states

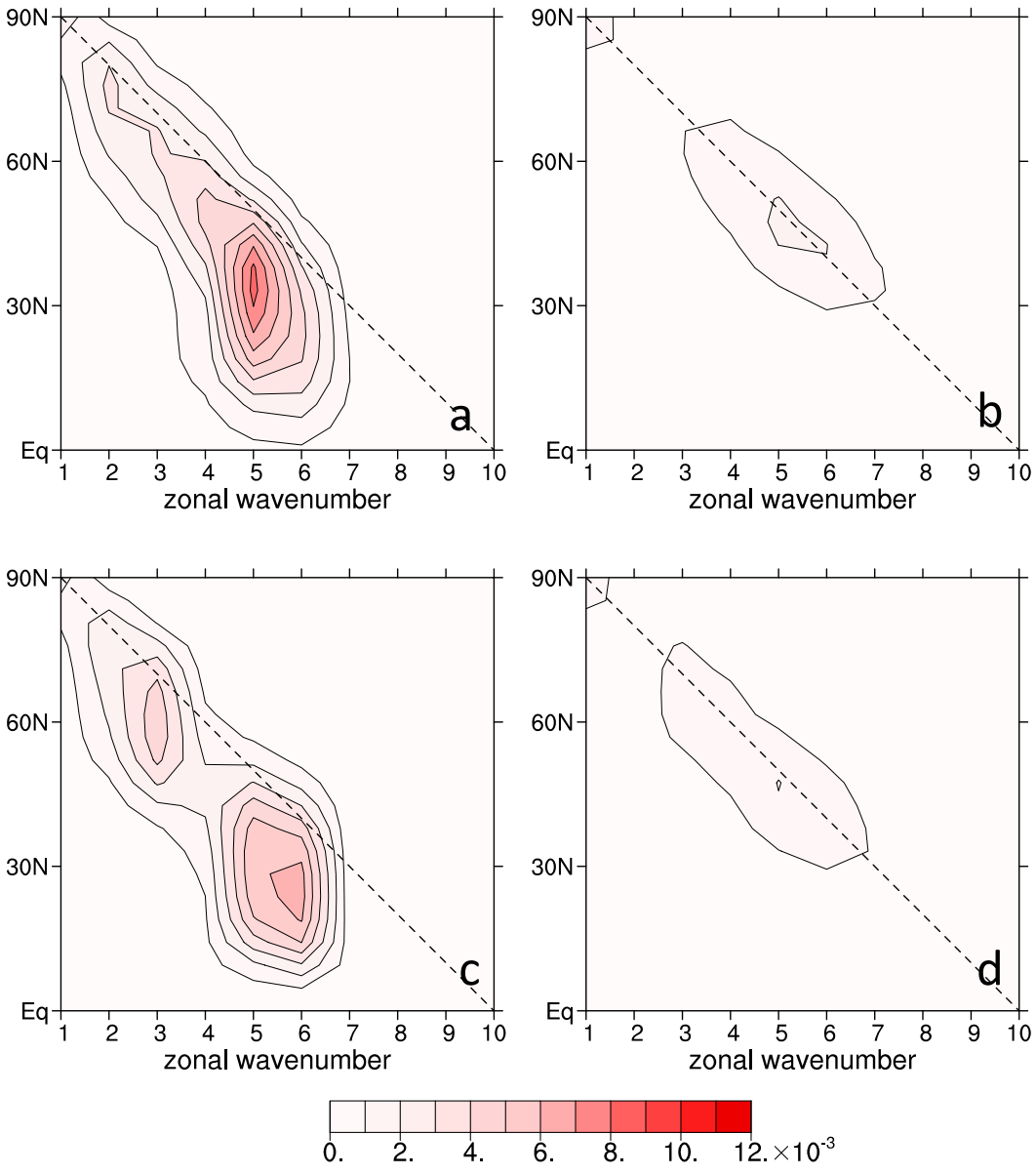

FIG. 12. Mean square Fourier amplitudes of one-point correlation maps, as in Fig. 5, but for v200 from a stochastically driven planetary wave model when it is linearized about climatological-mean conditions for reanalysis (a) DJF and (b) JJA. (c),(d) As in (a) and (b), respectively, but the basic states are truncated to retain only the zonal-mean component.

that consist of only the zonally symmetric component. Necessarily, longitudinal variations in statistical properties of the resulting one-point correlation maps are absent, but we find much of the true seasonal and latitudinal variation remains. For example, Fig. 14c shows the strong seasonality of xTC in midlatitudes in this case. Interestingly, though at some longitudes xTC is substantially weaker with a zonally symmetric basic state and at other longitudes it is stronger, overall there is only a minor weakening compared to the untruncated basic-state results of Fig. 11b. This fact is quantified by the values plotted on the right sides of Figs. 11b and 14, which are the RMS of the longitudinally varying xTC values to their left. For example, the RMS of xTC in midlatitudes during January is 0.258 for the untruncated basic state, and for the zonally symmetric basic state it is 0.246.[1]

[1] When we repeat our linear calculations using climatological means from CAM5 as basic states, this is the one result that is substantially different. In that case, the overall strength of xTC is much stronger for an untruncated basic state than for a zonally symmetric basic state.

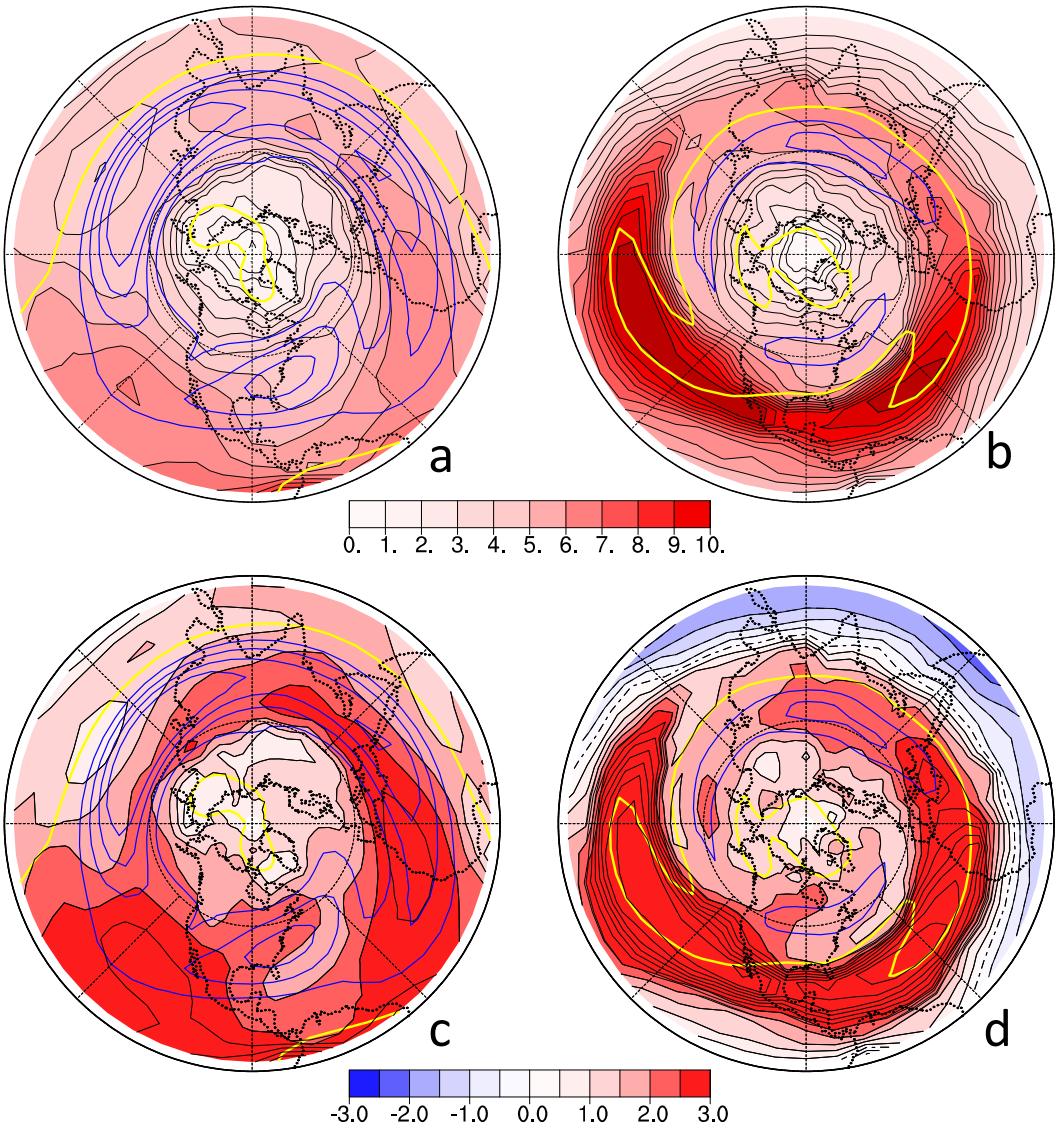

FIG. 13. Average local zonal wavenumber of one-point correlation maps, as in Fig. 6, but for v200 from a stochastically driven planetary wave model when it is linearized about climatological-mean conditions for reanalysis (a) DJF and (b) JJA. (c),(d) As in (a) and (b), respectively, but with values derived from the stationary wavenumber of solid-body rotation subtracted.

Finally, we find that the zonal-mean component of mean states is not sufficient to reproduce some of the most important features in the spectral distributions of variance seen in Figs. 5, 12a, and 12b. For zonal-mean basic states, the corresponding plots (Figs. 12c,d) do have the generally smaller scales at a given latitude during summer seen in more complete systems. (This is not surprising given our earlier discussion of seasonality in very simple linear models.) But zonal-mean basic states do not produce the dominance of zonal wavenumber-5 teleconnections during DJF. Instead, wave 6 is prevalent at the latitude of the jet core. This discrepancy is because the wavenumber-5 features that actually dominate there in winter exist in the core of the Asian subtropical jet (Figs. 6a, 13a), while the weaker zonally averaged jet supports smaller-scale waves. Indeed, when we make plots like those in Fig. 12 for linear solutions with basic states truncated at zonal wavenumber 2, then the correct prevalent scales are generated.

6. Summary and discussion

We have examined the seasonal dependence of the location, strength, zonal extent, and scale of upper-tropospheric teleconnection patterns in order to

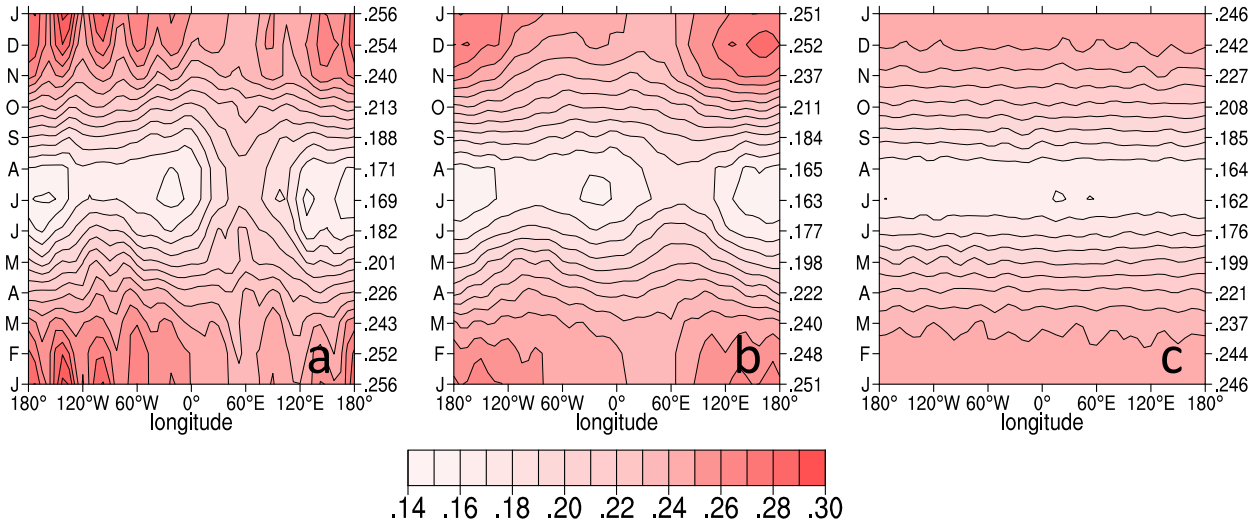

FIG. 14. Midlatitude-average extended teleconnectivity for solutions to a planetary wave model, as in Fig. 11b, but using basic states that are truncated beyond zonal wavenumbers (a) 5, (b) 2, and (c) 0. Values on the right vertical axis of each panel show the RMS of the plotted midlatitude-average xTC values for that month.

quantitatively estimate the effect that the climatological-mean jets have on teleconnections in their vicinity through their role as waveguides for Rossby waves. Based on statistical properties of one-point correlation maps of subseasonal meridional wind in reanalysis and AGCM Northern Hemisphere datasets, we have found that:

1) Throughout the year, base points near the core of the mean jets are associated with teleconnection patterns that are unusually strong and that produce covariability between widely separated regions. Being trapped in the jets, these patterns tend to be primarily oriented in the zonal direction.
2) Waveguide-induced teleconnections are much stronger and composed of larger-scale features in winter than summer, with zonal wavenumber 5 being the dominant scale in winter, while wavenumber 6 increases in prominence near the jet core during summer.
3) The strength, span, and scale of waveguide teleconnections during the transition seasons are intermediate between their winter and summer values and vary during the course of these seasons. The transition seasons are more like winter than summer in that, during the cool months, the strongest teleconnections occur for base points located in one broad swath, while in summer they are in two separate regions.
4) Throughout the year, within the waveguides there are alternating regions of relatively high and low covariability with the rest of the extratropics. The longitudes of these regions shift only gradually during the entire cool season while occurring at a different set of longitudes during summer. In winter and summer, these local maxima in extended teleconnectivity are a reflection of one and two of the strongest waveguide teleconnection patterns, respectively.

The first three of these attributes are qualitatively in line with the impact of the climatological-mean state, and in particular of the mean jets, expected from linear theory. Another factor that can potentially influence the structure of subseasonal and longer fluctuations is the structure of heating anomalies instigated by events external to the atmosphere (e.g., SST anomalies). For example, it is possible that a particular, recurring SST structure might preferentially excite a strong response in the waveguide. The fact that the AGCM experiment we analyzed contains no SST anomalies yet had nearly identical teleconnection properties to those in nature indicates they are not an important contributor to the properties we have identified. Even more indicative that forcing structure is not essential and that mean-state influences produce the striking properties of teleconnections associated with the mean jets is the remarkable similarity we found between those characteristic in nature and the AGCM and in solutions to a linear planetary wave model driven by forcing that had no organized structure. For these reasons we feel justified in designating these teleconnections as being "waveguide induced," which is to say they owe their existence to the mean-jet waveguides.

Though linearized dynamics did prove to be sufficient to produce most of the teleconnection characteristics we quantified, experiments with the linear model did indicate that the theories we discussed in the introduction are not sufficient to explain all aspects of these properties. Those theories assume basic states that vary slowly in space, but the experiments indicated that some properties, including

the spatial variations in teleconnection strength within the waveguide and the prominence of certain zonal scales in waveguide teleconnections, relied on basic states that varied on about the same scales as the perturbations. One interpretation of our linear solutions is that certain structures, in particular some in the waveguide, have natural frequencies that are close to zero and are thus preferentially excited by low-frequency forcing (Branstator 1985). Which of these structures is most resonant depends on whether the basic state includes the smaller-scale waves.

One implication of our results is that, from the covariability perspective of our study, ''circumglobal'' is an appropriate designation for some teleconnection patterns during NH winter, but probably not during NH summer. It is for this reason that we feel ''waveguide induced'' rather than ''circumglobal'' may be the more appropriate term in many circumstances for zonally oriented patterns of covariability that have extended zonal extent. We do recognize, however, that some of the choices we have made probably decreased the zonal extent of some of the teleconnection maps we considered. For example, in results not shown in this paper, we have found that the strength and span of teleconnections in CAM5 are increased somewhat if one considers values longer than the 20-day means on which much of our analysis of nature has been based. In the most extreme case, when 90-day means are used, some DJF patterns related to the one in Fig. 2a have truly circumglobal spans, but the span of the leading JJA pattern increases by only about 10%, so it still reaches less than halfway round the globe. Also, as mentioned in section 4, our choice to combine data into 3-month seasons when analyzing nature appears to have weakened xTC slightly, presumably because the waveguide patterns change somewhat during these seasons. And as we have mentioned, forcing by SST anomalies could potentially preferentially excite waveguide patterns, thus causing them to be more prominent in all seasons, but since we employed subseasonal fluctuations, this effect has been minimized. Also, as the analyses of Branstator (2002) and Ding and Wang (2005) have demonstrated, patterns trapped in the waveguides tend to have a zonally symmetric component, which our analysis of v200 does not capture. This component is not produced by the dynamical waveguide mechanisms that we have discussed, but it can add substantially to covariability, as is evident in Ding and Wang's summer jet-trapped geopotential pattern.

The final point we would like to make is that, though analyzing geopotential rather than meridional wind can enhance measures of covaribility because it includes a zonally symmetric component, as explained in appendix A, it is less effective for identifying variability shaped by the traditional waveguide mechanism. Indeed, in calculations not described here, when we have repeated some of our analysis using the zonally asymmetric component of geopotential, the strongest teleconnections, as measured by extended teleconnectivity, are no longer confined to the jet stream waveguides. Instead, during winter, the locations with strongest extended teleconnectivity are the centers of action of the Pacific–North America pattern, and in summer they are regions where a subtropical zonal wavenumber-1 feature predominates. For zonally asymmetric geopotential, base points within the mean jets are, in fact, often associated with zonally oriented teleconnections, but they are weaker than what we have displayed for meridional wind.

Acknowledgments. The authors appreciate helpful discussions with J. Tribbia, J. Wallace, C. Deser, and I. Simpson, as well as Andrew Mai's careful execution of the CAM5 experiments. GB acknowledges support by NOAA MAPP NA14OAR4310224 and NASA NEWS via NNX13AH92G. HT was supported by the Regional and Global Climate Modeling Program of the U.S. Department of Energy's Office of Science, Cooperative Agreement DE-FC02-97ER62402.

APPENDIX A

Properties of v Teleconnections

One-point correlation plots based on v should contrast in various ways with corresponding plots for streamfunction or geopotential. First, through consideration of a Fourier representation of streamfunction, it is apparent that v, which is proportional to the zonal derivative of streamfunction, gives more weight to smaller scales, which Fig. 1 indicates are likely to be confined to the core of the jets. Second, consideration of the linear barotropic vorticity equation in Mercator coordinates, as given by Hoskins and Karoly's (1981) Eq. (5.9), indicates the group velocity of v disturbances will be more zonally oriented and stronger than the group velocity of streamfunction. Taking the zonal derivative of that equation produces an equation for perturbation v that is formally identical to the equation for streamfunction. Hence, the same expressions that apply to the group velocity for stationary streamfunction anomalies also apply to v anomalies. In particular, the slope of rays is l/k, where k and l are the zonal and meridional wavenumber, respectively, of plane wave disturbances. Therefore, stationary disturbances in the v field, with their bias toward large k, will tend to be more zonally oriented. Also, since the group velocity of v (as well as of streamfunction) stationary disturbances is $2ku_M/K_s$, the scale bias of v will produce larger group velocities and, consequently, perturbations that propagate farther before decaying.

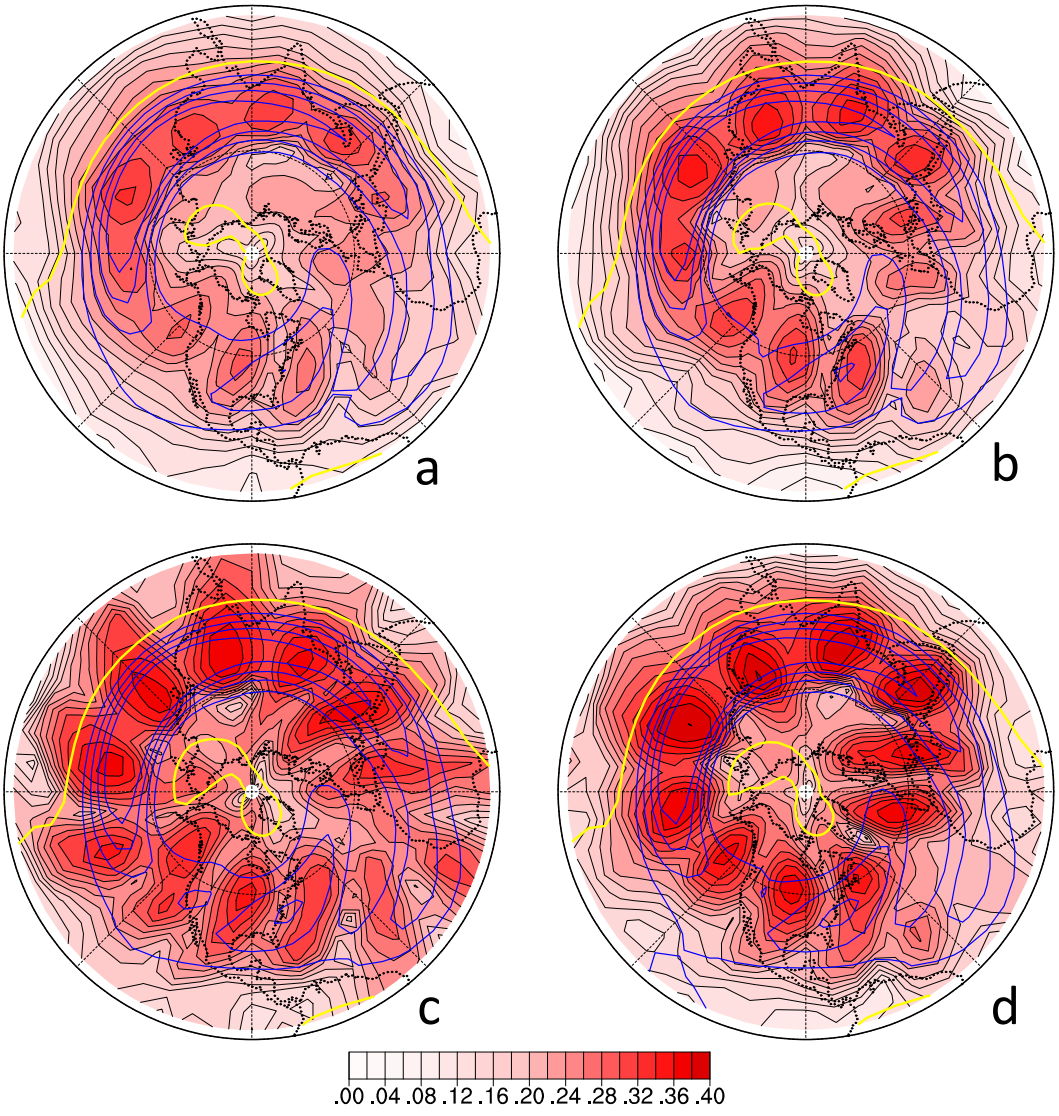

FIG. B1. Extended teleconnectivity of (a),(b) two 60-yr subsamples of subseasonal fluctuations of 20-day-average v200 during DJF of a CAM5 control integration and (c),(d) two 60-yr subsamples of subseasonal fluctuations of 30-day averages during January of the same experiment (59×5 v200 v200 fields contribute to each DJF plot and 60×1 fields contribute to each January plot). Overlaid are contours of u200 averaged for the same subsample used in the calculation of xTC.

APPENDIX B

Consequences of Small Samples

To assess uncertainties in features on maps of extended teleconnectivity for the reanalysis dataset, we take advantage of the 1000-yr dataset for CAM5 and the fact that its teleconnection properties match many of the attributes we have analyzed in nature. As surrogates for the 57-yr sample available for nature, we use 20 subsamples of the AGCM dataset, each consisting of 60 randomly drawn years. We then calculate xTC for each NH base point for each of these subsamples in the identical way that it was found for the v200 reanalysis dataset. To the eye, when we do this for DJF seasons consisting of five 20-day averages, each of the resulting 20 maps has a similar geographical distribution of xTC, though amplitudes vary somewhat from map to map. To be more quantitative, we calculate the RMS difference between each pair of these maps, and in Figs. B1a and B1b we show the two that are most different. Given the one-to-one correspondence between almost every feature on this pair, we conclude that we can be confident about the features we have discussed when considering Fig. 3a.

By contrast, if we repeat this procedure using monthly means from January, then the two maps that are most different are the ones shown in Figs. B1c and B1d. In this case, with about 5 times fewer independent samples contributing to each chart, there are substantial differences in the placement and structure of many features.

For other seasons, there is somewhat more uncertainty so that, for example, the exact longitude of local maxima of xTC cannot be determined, even when using five 20-day means to represent each year. This is especially true for spring and fall. It is for this reason that we rely on the AGCM dataset when examining the full seasonal cycle and 20-day averages when plotting xTC for winter and summer for nature. Uncertainties for spectra (e.g., Fig. 5) are smaller, so we can trust the seasonality we discuss for those results.

REFERENCES

Ambaum, M. H. P., B. J. Hoskins, and D. B. Stephenson, 2001: Arctic Oscillation or North Atlantic Oscillation? *J. Climate*, **14**, 3495–3507, doi:10.1175/1520-0442(2001)014<3495:AOONAO>2.0.CO;2.

Ambrizzi, T., B. J. Hoskins, and H.-H. Hsu, 1995: Rossby wave propagation and teleconnection patterns in the Austral winter. *J. Atmos. Sci.*, **52**, 3661–3672, doi:10.1175/1520-0469(1995)052<3661:RWPATP>2.0.CO;2.

Barnston, A. G., and R. E. Livezey, 1987: Classification, seasonality and persistence of low-frequency atmospheric circulation patterns. *Mon. Wea. Rev.*, **115**, 1083–1126, doi:10.1175/1520-0493(1987)115<1083:CSAPOL>2.0.CO;2.

Branstator, G., 1983: Horizontal energy propagation in a barotropic atmosphere with meridional and zonal structure. *J. Atmos. Sci.*, **40**, 1689–1708, doi:10.1175/1520-0469(1983)040<1689:HEPIAB>2.0.CO;2.

——, 1985: Analysis of general circulation model sea-surface temperature anomaly simulations using a linear model. Part II: Eigenanalysis. *J. Atmos. Sci.*, **42**, 2242–2254, doi:10.1175/1520-0469(1985)042<2242:AOGCMS>2.0.CO;2.

——, 1990: Low-frequency patterns induced by stationary waves. *J. Climate*, **47**, 629–649, doi:10.1175/1520-0469(1990)047<0629:LFPIBS>2.0.CO;2.

——, 2002: Circumglobal teleconnections, the jet stream waveguide, and the North Atlantic Oscillation. *J. Climate*, **15**, 1893–1910, doi:10.1175/1520-0442(2002)015<1893:CTTJSW>2.0.CO;2.

——, and J. Frederiksen, 2003: The seasonal cycle of interannual variability and the dynamical imprint of the seasonally varying mean state. *J. Atmos. Sci.*, **60**, 1577–1591, doi:10.1175/3002.1.

Chen, T.-C., 2002: A North Pacific short-wave train during the extreme phases of ENSO. *J. Climate*, **15**, 2359–2376, doi:10.1175/1520-0442(2002)015<2359:ANPSWT>2.0.CO;2.

Deser, C., 2000: On the teleconnectivity of the "Arctic Oscillation." *Geophys. Res. Lett.*, **27**, 779–782, doi:10.1029/1999GL010945.

Ding, Q., and B. Wang, 2005: Circumglobal teleconnections in the Northern Hemisphere summer. *J. Climate*, **18**, 3483–3505, doi:10.1175/JCLI3473.1.

——, ——, J. Wallace, and G. Branstator, 2011: Tropical–extratropical teleconnections in boreal summer: Observed interannual variability. *J. Climate*, **24**, 1878–1896, doi:10.1175/2011JCLI3621.1.

Harnik, N., G. Messori, R. Caballero, and S. Feldstein, 2016: The circumglobal North American wave pattern and its relation to cold events in eastern North America. *Geophys. Res. Lett.*, **43**, 11 015–11 023, doi:10.1002/2016GL070760.

Hoskins, B. J., 1983: Dynamical processes in the atmosphere and the use of models. *Quart. J. Roy. Meteor. Soc.*, **109**, 1–21, doi:10.1002/qj.49710945902.

——, and D. Karoly, 1981: The steady linear response of a spherical atmosphere to thermal and orographic forcing. *J. Atmos. Sci.*, **38**, 1179–1196, doi:10.1175/1520-0469(1981)038<1179:TSLROA>2.0.CO;2.

——, and T. Ambrizzi, 1993: Rossby wave propagation on a realistic longitudinally varying flow. *J. Atmos. Sci.*, **50**, 1661–1671, doi:10.1175/1520-0469(1993)050<1661:RWPOAR>2.0.CO;2.

Hsu, H.-H., and S.-H. Lin, 1992: Global teleconnections in the 250-mb streamfunction field during the Northern Hemisphere winter. *Mon. Wea. Rev.*, **120**, 1169–1190, doi:10.1175/1520-0493(1992)120<1169:GTITMS>2.0.CO;2.

Hurrell, J., and Coauthors, 2013: The Community Earth System Model: A framework for collaborative research. *Bull. Amer. Meteor. Soc.*, **94**, 1339–1360, doi:10.1175/BAMS-D-12-00121.1.

Kay, J. E., and Coauthors, 2015: The Community Earth System Model (CESM) Large Ensemble Project: A community resource for studying climate change in the presence of internal climate variability. *Bull. Amer. Meteor. Soc.*, **96**, 1333–1349, doi:10.1175/BAMS-D-13-00255.1.

Kosaka, Y., H. Nakamura, M. Watanabe, and M. Kimoto, 2009: Analysis on the dynamics of a wave-like teleconnection pattern along the summertime Asian jet based on a reanalysis dataset and climate model simulations. *J. Meteor. Soc. Japan*, **87**, 561–580, doi:10.2151/jmsj.87.561.

Manola, I., F. Selten, H. de Vries, and W. Hazeleger, 2013: "Waveguidability" of idealized jets. *J. Geophys. Res. Atmos.*, **118**, 10 432–10 440, doi:10.1002/jgrd.50758.

Newman, M., and P. Sardeshmukh, 1998: The impact of the annual cycle on the North Pacific/North American response to remote low-frequency forcing. *J. Atmos. Sci.*, **55**, 1336–1353, doi:10.1175/1520-0469(1998)055<1336:TIOTAC>2.0.CO;2.

Petoukhov, V., S. Rahmstorf, S. Petri, and H. J. Schellnhuber, 2013: Quasiresonant amplification of planetary waves and recent Northern Hemisphere weather regimes. *Proc. Natl. Acad. Sci. USA*, **110**, 5336–5341, doi:10.1073/pnas.1222000110.

Rossby, C.-G., 1939: Relation between variations in the intensity of the zonal circulation of the atmosphere and displacements of the semi-permanent centers of action. *J. Mar. Res.*, **2**, 38–55, doi:10.1357/002224039806649023.

——, 1945: On the propagation of frequencies and energy in certain types of oceanic and atmospheric waves. *J. Meteor.*, **2**, 187–204, doi:10.1175/1520-0469(1945)002<0187:OTPOFA>2.0.CO;2.

Schubert, S., H. Wang, and M. Suarez, 2011: Warm season subseasonal variability and climate extremes in the Northern Hemisphere: The role of stationary Rossby waves. *J. Climate*, **24**, 4773–4792, doi:10.1175/JCLI-D-10-05035.1.

Teng, H., G. Branstator, H. Wang, G. A. Meehl, and W. M. Washington, 2013: Probability of U.S. heat waves affected by a subseasonal planetary wave pattern. *Nat. Geosci.*, **6**, 1056–1061, doi:10.1038/ngeo1988.

Wallace, J. M., and D. S. Gutzler, 1981: Teleconnections in the geopotential height field during the Northern Hemisphere winter. *Mon. Wea. Rev.*, **109**, 784–812, doi:10.1175/1520-0493(1981)109<0784:TITGHF>2.0.CO;2.

Watanabe, M., 2004: Asian jet waveguide and a downstream extension of the North Atlantic Oscillation. *J. Climate*, **17**, 4674–4691, doi:10.1175/JCLI-3228.1.

Yeh, T., 1949: On energy dispersion in the atmosphere. *J. Meteor.*, **6**, 1–16, doi:10.1175/1520-0469(1949)006<0001:OEDITA>2.0.CO;2.